Seismic attenuation beneath northeastern Japan: Constraints on mantle dynamics and arc magmatism

Junichi Nakajima,[1] Shuhei Hada,[1] Erika Hayami,[1,2] Naoki Uchida,[1] Akira Hasegawa,[1] Shoichi Yoshioka,[3] Toru Matsuzawa,[1] and Norihito Umino[1]

Received 27 May 2013; revised 8 October 2013; accepted 16 October 2013.

[1] We apply a three-step approach to estimate three-dimensional (3-D) P wave attenuation (Q_p^{-1}) structure beneath northeastern Japan. First, corner frequencies of earthquakes are determined using the spectral-ratio method for S-coda waves. Then, whole-path attenuation terms, t^*, and site-amplification factors are simultaneously estimated by a joint inversion. The set of t^* is finally inverted for 3-D attenuation structure. The results show that the mantle wedge has low attenuation in the fore arc and high attenuation in the back arc. A depth profile of Q_p^{-1} in the back-arc mantle is explained by attenuation expected for a two-dimensional (2-D) thermal model with $Q_p/Q_s = 2$ and grain sizes of 1 and 3 cm. However, an inclined high-attenuation zone observed in the back-arc mantle wedge, which is interpreted as an upwelling flow, shows higher attenuation than that calculated from the 2-D thermal model. The higher seismic attenuation is probably caused by the concentration of partial melt in the upwelling flow. A combined interpretation of seismic attenuation and velocity structures further suggests that the degree of partial melt in the upwelling flow varies along the arc and that volcanoes are clustered transverse to the arc, below which the upwelling flow contains a higher degree of melt. These observations indicate that magmatism is controlled by a mantle-wedge process that depends strongly on spatial variations in the degree of partial melt in the upwelling flow. Our results further imply the breakdown of hydrous minerals in a hydrous layer above the Pacific plate at a depth of ~120 km.

Citation: Nakajima, J., S. Hada, E. Hayami, N. Uchida, A. Hasegawa, S. Yoshioka, T. Matsuzawa, and N. Umino (2013), Seismic attenuation beneath northeastern Japan: Constraints on mantle dynamics and arc magmatism, *J. Geophys. Res. Solid Earth*, *118*, doi:10.1002/2013JB010388.

1. Introduction

[2] Subduction zones recycle hydrous minerals that are transformed by metamorphic processes into high-pressure and high-temperature minerals. Hydrous minerals in subducting oceanic lithosphere become unstable with increasing pressure and temperature, and dehydration reactions progressively occur, accompanied by the release of aqueous fluids into the overlying mantle wedge [e.g., *Hacker et al.*, 2003]. Aqueous fluids thus liberated to the mantle wedge can produce partial melting as a result of lowering of the solidus of peridotite, and the partial melts are then transported to below the Moho by convective flow, resulting in intensive arc magmatism in subduction zones [e.g., *Wiens et al.*, 2008].

[3] In northeastern (NE) Japan, the Pacific plate is subducting beneath the land area and the volcanic front runs through the middle of the arc (Figure 1a). There are strong contrasts between the fore-arc and back-arc sides; for example, in terrestrial heat flow [e.g., *Tanaka et al.*, 2004] and in ^{3}He/^{4}He ratios [e.g., *Sano and Nakajima*, 2008]. In addition, volcanoes are not distributed continuously along the volcanic front but form somewhat-isolated clusters striking transverse to the arc with along-arc gaps of 30–80 km (broken lines in Figure 1a) [*Tamura et al.*, 2002]. These surface manifestations with marked across- and along-arc variations suggest that a large-scale physical process controls present-day geochemical differentiation and arc magmatism.

[4] Seismic tomography studies beneath NE Japan have revealed the existence of an inclined low-velocity zone in the mantle wedge (Figure 1b), which interpreted as a mantle upwelling flow induced by the subduction of the Pacific plate [e.g., *Hasegawa et al.*, 1991; *Zhao et al.*, 1992, 2012; *Nakajima et al.*, 2001]. *Hasegawa and Nakajima* [2004] first identified the along-arc variation in S wave velocity for

Additional supporting information may be found in the online version of this article.

[1]Research Center for Prediction of Earthquakes and Volcanic Eruptions, Graduate School of Science, Tohoku University, Sendai, Japan.
[2]Japan Meteorological Agency, Tokyo, Japan.
[3]Research Center for Urban Safety and Security, Kobe University, Kobe, Japan.

Corresponding author: J. Nakajima, Research Center for Prediction of Earthquakes and Volcanic Eruptions, Graduate School of Science, Tohoku University, Sendai 9808578, Japan. (nakajima@aob.gp.tohoku.ac.jp)

2169-9313/13/10.1002/2013JB010388

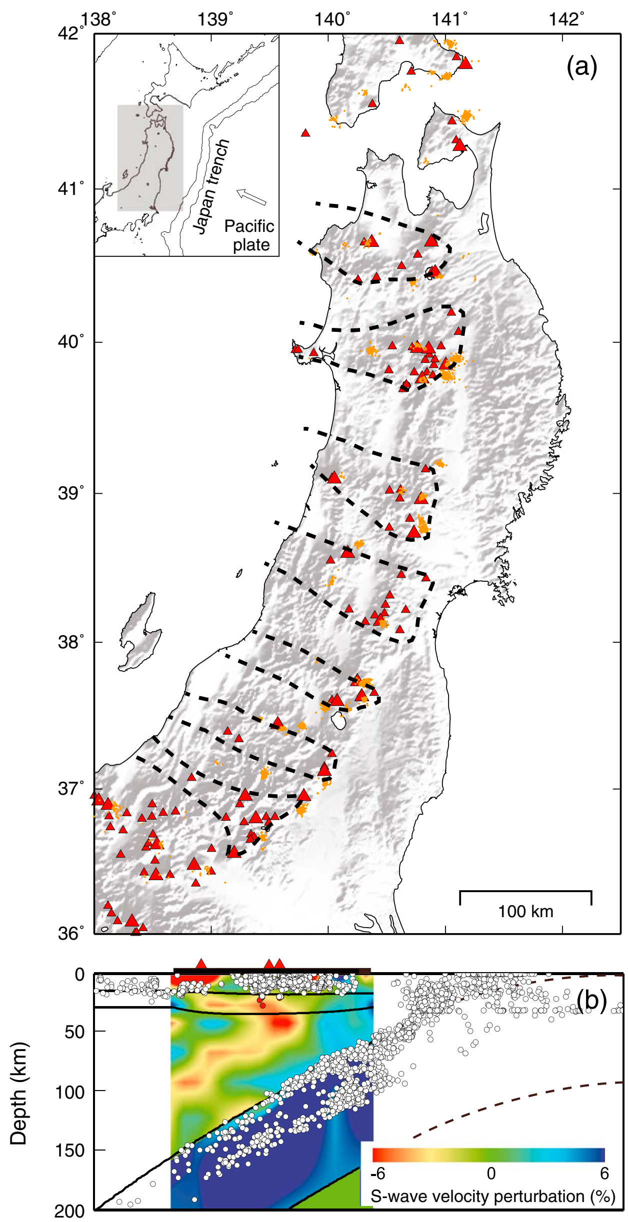

Figure 1. (a) Map of the study area with shaded topography. Large and small red triangles denote active and Quaternary volcanoes, respectively. Orange dots represent deep, low-frequency earthquakes that occurred around the continental Moho. Black dashed lines denote clustering of Quaternary volcanoes [*Tamura et al.*, 2002]. (b) Across-arc vertical cross section of *S* wave velocity perturbation along the latitude of 39° [*Nakajima et al.*, 2001]. Solid lines indicate the Conrad and Moho, and the upper surface of the Pacific plate. Black bars and red triangles on the top of each panel denote the land area and active volcanoes, respectively. White and red circles represent ordinary earthquakes and deep low-frequency earthquakes, respectively.

the upwelling flow, with an excellent correlation among areas of marked velocity reduction in the flow, clustering of Quaternary volcanoes, and distributions of deep, low-frequency earthquakes in the lower crust. Based on these observations, *Hasegawa and Nakajima* [2004] proposed a model that the heterogeneity in the upwelling flow has governed surface and subsurface magmatic activities.

[5] Seismic attenuation provides additional insights into ongoing magmatic processes in subduction zones, because higher-temperature environments or the existence of fluids may have different effects on seismic attenuation from on seismic velocity [e.g., *Karato*, 2003]. It is known that seismic attenuation in NE Japan shows a strong contrast between the fore-arc and back-arc mantle wedges [e.g., *Umino and Hasegawa*, 1984; *Matsuzawa et al.*, 1989; *Tsumura et al.*, 1996, 2000; *Ko et al.*, 2012; *Takahashi*, 2012]. A high attenuation is observed in the back-arc mantle wedge, whereas the fore-arc mantle shows low attenuation. *Takanami et al.* [2000] detected an area with strong attenuation ($Q_s^{-1} = \sim 0.013$) in the uppermost mantle beneath the volcanic front. Even though seismic attenuation has contributed to estimates of thermal structure in the mantle wedge [e.g., *Takanami et al.*, 2000; *Nakajima and Hasegawa*, 2003], the spatial resolution of attenuation structure is not as high as that of velocity structure because of the limitation of waveform data with high signal-to-noise (S/N) ratios. Therefore, it is essential to update three-dimensional (3-D) seismic attenuation models to improve our understanding of magmatism in subduction zones.

[6] This study estimates 3-D seismic attenuation structure beneath NE Japan using a large number of high-quality waveforms obtained at a dense seismograph network in Japan. The obtained seismic attenuation is interpreted based on temperature distributions and melt contents in the mantle wedge, and is then discussed in terms of arc magmatism and mantle dynamics.

2. Methodology

2.1. General Formulae

[7] Seismic attenuation has been estimated from the spectra of seismic waveforms. Following the approach outlined by *Scherbaum* [1990], a velocity amplitude spectrum for event *i* observed at station *m* can be expressed as

$$A_{im}(f) = 2\pi f S_i(f) I_m(f) R_m(f) B_{im}(f) F_{im} \tag{1}$$

where f is the frequency, $S_i(f)$ is the source spectrum, $I_m(f)$ is the instrument response, $R_m(f)$ is the site-amplification factor, $B_{im}(f)$ describes the attenuation along a raypath between event *i* and station *m*, and F_{im} represents frequency-independent terms associated with the radiation pattern, geometrical spreading, and other static effects. The attenuation term is given by

$$B_{im}(f) = \exp\left[-\pi f t^*_{im}(f)\right] \tag{2}$$

where $t^*_{im}(f)$ is a frequency-dependent attenuation term along a raypath from event *i* to station *m*. With an attenuation term at 1 Hz, $t^*_{0\_im}$, $t^*_{im}(f)$ is expressed as

$$t^*_{im}(f) = t^*_{0\_im} f^{-\alpha} \tag{3}$$

where α represents a frequency-dependent factor with a range of 0–1. Given instrumental responses and an ω^2 source model [*Brune*, 1970], the velocity amplitude spectrum is expressed as

$$A_{im}(f) = \Omega_{im} \frac{f}{1 + \left(\frac{f}{f_{ci}}\right)^2} R_m(f) \exp\left(-\pi f^{1-\alpha} t^*_{0\_im}\right) \quad (4)$$

where f_{ci} represents the source corner frequency of event i. Here we incorporate frequency-independent terms into an operator, Ω_{im}. With equation (4), the source spectrum, site-amplification factor, and attenuation term at 1 Hz can be determined from spectra observed for many earthquakes.

2.2. Strategy to Minimize Trade-Off Among Parameters

[8] Site-amplification factors, $R_m(f)$, are expressed as a constant term, $t^*_{station}$ [e.g., *Rietbrock*, 2001; *Eberhart-Phillips and Chadwick*, 2002] or they are estimated from the residuals between observed and theoretical spectra for each station [e.g., *Stachnik et al.*, 2004]. These procedures are valid when site-amplification factors depend little on frequency, but they may introduce systematic errors in the estimates of the attenuation term when site-amplification factors show a significant frequency dependence, as is commonly observed [e.g., *Iwata and Irikura*, 1988; *Boatwright et al.*, 1991; *Tsumura et al.*, 2000]. Therefore, the precise estimates of site-amplification factors are required for reliable estimates of the attenuation term.

[9] Apart from site-amplification factors, the parameters $t^*_{0\_im}$, f_{ci}, and Ω_{im} are often simultaneously determined from the shape of spectral amplitudes [e.g., *Eberhart-Phillips and Chadwick*, 2002]. However, there is a large trade-off between f_{ci} and $t^*_{0\_im}$ because both parameters affect spectral falloff [e.g., *Ko et al.*, 2012]. Generally, a value of f_{ci} higher than the optimum value will yield a higher value of $t^*_{0\_im}$, and vice versa. For stable and precise estimates of seismic attenuation, it is also essential to determine f_{ci} independently of $t^*_{0\_im}$.

[10] This study tries to minimize these trade-off problems and estimates 3-D seismic attenuation structures using a three-step approach. First, we estimate f_{ci} using spectral ratios of S-coda waves for collocated earthquakes recorded at common stations. One of the important advantages of the use of coda waves rather than direct waves is that coda waves provide more stable amplitude ratios than do direct waves [e.g., *Mayeda et al.*, 2007]. Second, we determine $t^*_{0\_im}$, $R_m(f)$, and Ω_{im} by a joint inversion of spectral amplitudes that are corrected for the source spectrum of each earthquake. Third, we invert observed values of $t^*_{0\_im}$ to estimate 3-D attenuation structure in NE Japan.

3. Corner Frequencies

3.1. Method

[11] It is known that the coda wave amplitudes become insensitive to the radiation pattern and medium heterogeneity and depend only on a lapse time and frequency, when a lapse time measured from the source origin time is longer than twice the direct S wave travel time (t_s) [e.g., *Sato and Fehler*, 1998]. This means that coda waves at a lapse time of $>2t_s$ do not involve complicated factors such as the source radiation pattern and medium heterogeneities along scattered rays. These characteristics have been used to estimate source parameters from spectral ratios of S-coda waves [e.g., *Takahashi et al.*, 2005; *Mayeda et al.*, 2007].

[12] The ratio of coda spectral amplitudes is calculated at common station m for collocated events i and j. The calculated spectral ratio has two corners together with flat levels at low- and high-frequency limits. When the magnitude of event i is larger than that of event j, corners at lower and higher frequencies correspond to f_c of events i and j, respectively. The optimum values of the corner frequencies of the two earthquakes, f_{ci} and f_{cj}, and the ratio of spectral levels are determined by a grid search technique for a frequency range of 1–32 Hz with a one-third-octave bandwidth, by minimizing the misfits between observed and theoretical spectral ratios for common stations. In the grid search, we use an interval of 0.2 for f_c and an adaptive increment for the ratio of spectral levels. This method determines f_c of an earthquake for every pair of earthquakes.

3.2. Data

[13] We collected velocity waveform data of 1432 shallow earthquakes with focal depths (H) of <40 km and 1608 intermediate-depth earthquakes with $H \geq 40$ km that occurred from January 2003 to February 2013 beneath the land area of NE Japan. Magnitudes of the earthquakes range from 2.5 to 5.0. Because the source radiation pattern and medium heterogeneities can be eliminated when coda waves from a pair of earthquakes have comparable propagation path effects, spectral ratios were calculated separately for shallow and intermediate-depth earthquakes. In the calculation, we considered earthquake pairs with interevent separations, D, of less than 40 km for shallow earthquakes, and less than the average focal depth of an earthquake pair for intermediate-depth earthquakes.

[14] We analyzed spectral amplitudes calculated from the transverse component of waveforms. Spectral amplitudes were calculated for S-coda waves with a time window of 10 s taken at twice the theoretical S wave travel time for the 1-D seismic velocity model [*Hasegawa et al.*, 1978]. Noise spectral amplitudes were calculated in the same manner but with a window length of 5 s before the onset of P waves. Only a frequency range with an S/N ratio of ≥3 was included in the analysis. Then, spectral ratios were calculated for available earthquake pairs at common stations. We limited earthquake pairs to those with a magnitude difference of at least 0.5 to ensure stable measurements of corner frequencies. In cases where spectral ratios were observed at five or more common stations for an earthquake pair, the average spectral ratio was calculated. Then, an ω^2 source model [*Brune*, 1970] was fitted to the averaged spectral ratio and values of f_c for the earthquake pair were estimated. In cases where values of f_c for an earthquake were determined from five or more pairs of earthquakes, we calculated the average f_c for that earthquake and used it in the subsequent analysis.

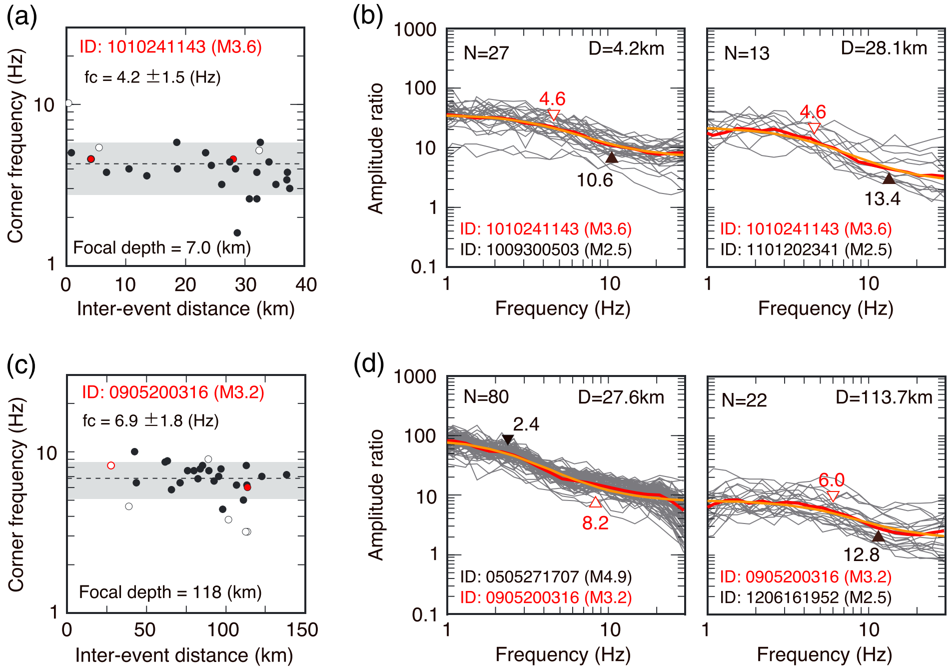

Figure 2. Examples of the estimates of corner frequencies (f_c) using the spectral ratio method for two target earthquakes (ID:1010241143 and ID:0905200316). (a) Estimated f_c versus interevent distance for an M3.6 shallow earthquake. The average value of f_c and its standard deviation are indicated by a dashed line and a gray shaded band, respectively. Filled and open circles denote that the target earthquake is paired with smaller and larger earthquakes in the spectral ratio, respectively. Red circles show a pair of earthquakes for which examples of spectral ratios are shown in Figure 2b. (b) Examples of spectral ratios for the target earthquake with respect to two earthquakes. Gray and red lines denote spectral ratios for various stations and the stacked spectral ratio, respectively. The orange line denotes the theoretical spectral ratio that best fits the observations. Values of f_c estimated for the target and other earthquakes are shown by red and black triangles with f_c values, respectively. Interevent distances (D) and the number of stations (N) available for taking spectral ratios are shown in the panel. (c) Estimated f_c versus interevent distance for an M3.2 intermediate-depth earthquake. Red circle and white circle outlined by red show a pair of earthquakes for which examples of spectral ratios are shown in Figure 2d. Symbols are the same as in Figure 2a. (d) Examples of spectral ratios for the target earthquake with respect to two earthquakes. Symbols are the same as in Figure 2b.

3.3. Results

[15] We obtained f_c of 998 shallow and 1230 intermediate-depth earthquakes. Figure 2a shows that for a shallow earthquake of M3.6, f_c can be stably estimated for different pairs of earthquakes with 4.2 ± 1.5 Hz (circles in Figure 2a). Spectral ratios of the M3.6 earthquake with respect to other earthquakes show that the spectral ratio method works well not only for a pair of earthquakes with a short interevent distance but also for a pair with a larger interevent distance (Figure 2b). For an intermediate-depth earthquake of M3.2, we estimated a value of f_c of 6.9 ± 1.8 Hz (Figure 2c). For earthquake pairs with larger interevent distances, f_c was stably determined (Figure 2d). The maximum interevent distance used in this study is larger than the criteria used in previous studies [e.g., *Mayeda et al.*, 2007], but the results of our analysis show that f_c can be determined by coda spectral ratios for earthquake pairs even in larger interevent distances.

[16] A plot of the obtained f_c versus seismic moment is presented in Figure 3. Static stress drops were calculated with the formula of *Eshelby* [1957] using the source radius of earthquakes estimated by a circular crack model [*Sato and Hirasawa*, 1973]. The calculated stress drops range mainly from 1 to 100 MPa with the relationship $M_0 \propto f_c^{-3}$. These stress drops are compatible with stress drops of 1–40 MPa estimated for small- to medium-sized earthquakes in NE Japan [e.g., *Uchida et al.*, 2007; *Ko et al.*, 2012; *Takahashi*, 2012; *Nakajima et al.*, 2013a,2013b]. Spatial and depth variations in stress drops of earthquakes may be of interest in terms of the characterization of source processes or the strength of faults, but their detailed discussion is beyond the scope of this paper because the quantitative analysis of stress drops requires precise estimates of the seismic moment of each earthquake.

4. Site-Amplification Factors and Attenuation Term

4.1. Method

[17] Once f_{ci} is estimated, equation (4) is modified as follows:

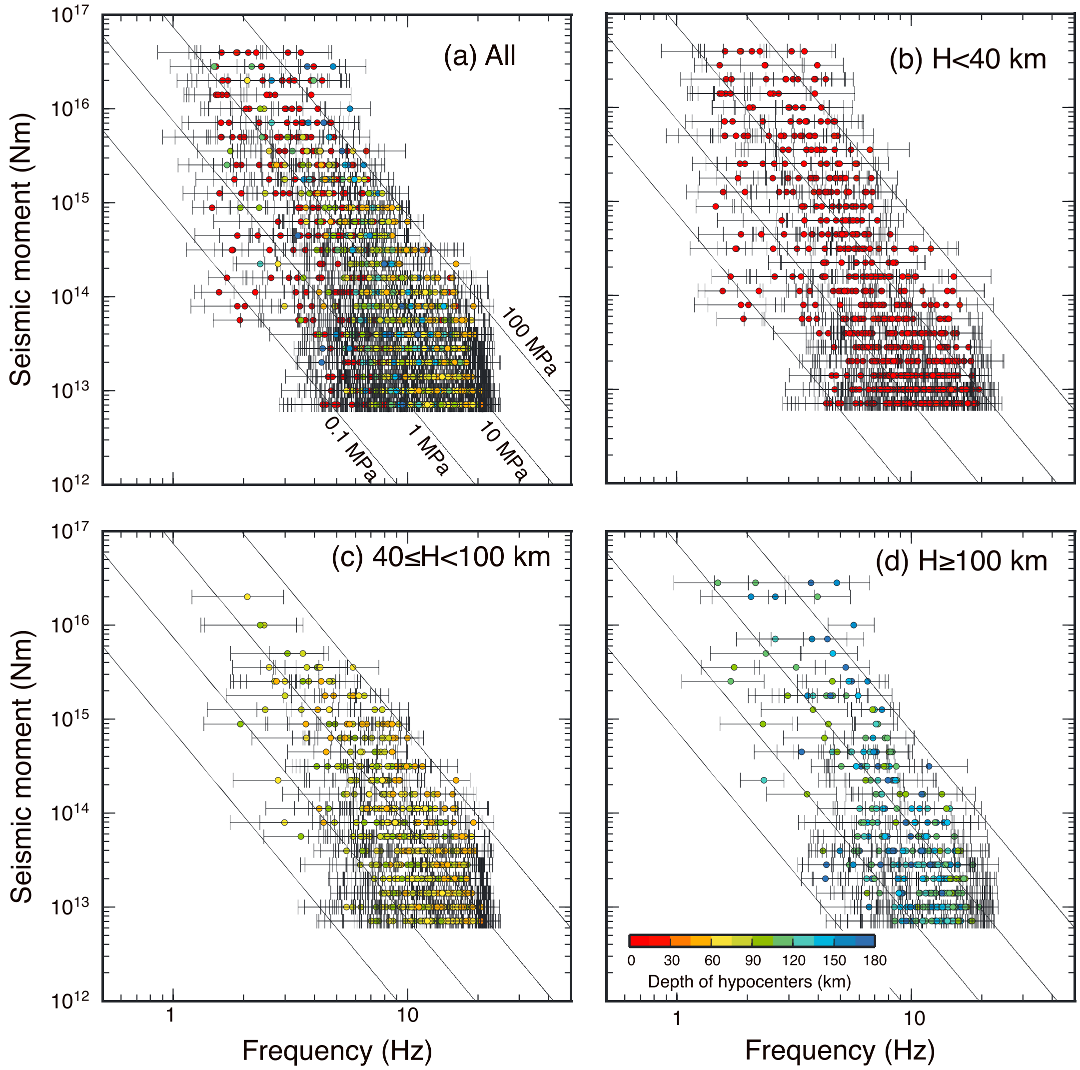

Figure 3. Plots of S wave corner frequency (f_c) versus seismic moment for (a) all earthquakes, (b) earthquakes with focal depths (H) of <40 km, (c) earthquakes with H of 40–100 km, and (d) earthquakes with H of ≥100 km. Circles and bars denote the average value of f_c and its standard deviation. Colors are proportional to the focal depth of the hypocenters. Solid lines denote iso-value lines of static stress drops at 0.1, 1, 10, and 100 MPa. The seismic moment, M_0, is estimated from $\log M_0 = 1.5M_{\mathrm{jma}} + 9.1$, where M_{jma} is the magnitude determined by the Japan Meteorological Agency.

$$\frac{1+\left(\frac{f}{f_{ci}}\right)^2}{f} A_{im}(f) = \Omega_{im} \exp\left(-\pi f^{1-\alpha} t^*_{0\_im}\right) R_m(f) \quad (5)$$

[18] The left-hand term can be evaluated from observations at each frequency, and the unknown parameters are all included in the right-hand term. Equation (5) is linearized by taking logarithms,

$$\log O_{im}(f) = \log\Omega_{im} + G(f) t^*_{0\_im} + \log R_m(f) \quad (6)$$

where $O_{im}(f) = \frac{1+\left(\frac{f}{f_{ci}}\right)^2}{f} A_{im}(f)$, $G(f) = -\pi f^{1-\alpha}\log(e)$, and e is Napier's number. Given no intrinsic attenuation in medium and frequency-independent site-amplification factors, the left-hand term of equation (6) becomes constant in the frequency domain. For real data, the left-hand term of equation (6) is inclined and has troughs and peaks as a result of intrinsic attenuation and frequency-dependent site-amplification factors. Such deviations from the flat level can be used to constrain seismic attenuation and site-amplification factors. Because Ω_{im} and $t^*_{0\_im}$ are represented for each raypath and $R_m(f)$ is estimated for each station, we can write equation (6) as a set of equations for many earthquakes at one station. Consequently, the observation equations at station m can be described in matrix form as follows:

$$
\begin{bmatrix}
\log O_{1m}(f_1)\\
\log O_{1m}(f_2)\\
\vdots\\
\log O_{1m}(f_K)\\
\log O_{2m}(f_1)\\
\log O_{2m}(f_2)\\
\vdots\\
\log O_{2m}(f_K)\\
\vdots\\
\vdots\\
\log O_{Nm}(f_1)\\
\log O_{Nm}(f_2)\\
\vdots\\
\log O_{Nm}(f_K)
\end{bmatrix}
=
\begin{bmatrix}
1 & 0 & \cdots & 0 & G(f_1) & 0 & \cdots & 0 & 1 & 0 & \cdots & 0\\
1 & 0 & \cdots & 0 & G(f_2) & 0 & \cdots & 0 & 0 & 1 & \cdots & 0\\
\vdots & \vdots & \cdots & \vdots & \vdots & \vdots & \cdots & \vdots & \vdots & \cdots & \cdots & \vdots\\
1 & 0 & \cdots & 0 & G(f_K) & 0 & \cdots & 0 & 0 & \cdots & \cdots & 1\\
0 & 1 & \cdots & 0 & 0 & G(f_1) & \cdots & 0 & 1 & 0 & \cdots & 0\\
0 & 1 & \cdots & 0 & 0 & G(f_2) & \cdots & 0 & 0 & 1 & \cdots & 0\\
\vdots & \vdots & \cdots & \vdots & \vdots & \vdots & \cdots & \vdots & \vdots & \vdots & \cdots & \vdots\\
0 & 1 & \cdots & 0 & 0 & G(f_K) & \cdots & 0 & 0 & 0 & \cdots & 1\\
\vdots & \cdots & \cdots & \vdots & \vdots & \vdots & \cdots & \vdots & \vdots & \vdots & \cdots & \vdots\\
\vdots & \cdots & \cdots & \vdots & \vdots & \vdots & \cdots & \vdots & \vdots & \vdots & \cdots & \vdots\\
0 & \cdots & \cdots & 1 & 0 & 0 & \cdots & G(f_1) & 1 & 0 & \cdots & 0\\
0 & \cdots & \cdots & 1 & 0 & 0 & \cdots & G(f_2) & 0 & 1 & \cdots & 0\\
\vdots & \cdots & \cdots & \vdots & \vdots & \vdots & \cdots & \vdots & \vdots & \vdots & \cdots & \vdots\\
0 & \cdots & \cdots & 1 & 0 & 0 & \cdots & G(f_K) & 0 & 0 & \cdots & 1
\end{bmatrix}
\begin{bmatrix}
\log\Omega_{1m}\\
\log\Omega_{2m}\\
\vdots\\
\log\Omega_{Nm}\\
t^*_{0\_1m}\\
t^*_{0\_2m}\\
\vdots\\
t^*_{0\_Nm}\\
\log R_m(f_1)\\
\log R_m(f_2)\\
\vdots\\
\log R_m(f_K)
\end{bmatrix}
\quad (7)
$$

where N is the number of earthquakes observed at station m and K is the number of frequencies in a range of 1–32 Hz with a one-third octave bandwidth. Because the parameters Ω_{im} and $R_m(f)$ control the level of observed spectra, we introduce an additional constraint to equation (7), which is that the average of site-amplification factors in the logarithm is zero, written as

$$\frac{1}{K}\sum_{k=1}^{K}\log R_m(f_k) = 0 \quad (8)$$

[19] We solve equations (7) and (8) in the least squares sense, and determine Ω_{im} and $t^*_{0\_im}$ for each raypath and $R_m(f)$ for each station. It is noted that $R_m(f)$ estimated in this study represents relative site amplifications over a frequency range of interest.

4.2. Data and Analysis

4.2.1. Data

[20] We used waveform data for the 998 shallow and 1230 intermediate-depth earthquakes whose f_c were determined in section 3. For each waveform, spectral amplitudes were calculated from the vertical component for *P* waves and from the transverse component for *S* waves with a window length of 2.56 s from the onset of each wave. Noise spectral amplitudes were calculated with a window length of 2.56 s before the arrival time of each wave. In this analysis, we used only seismograms observed at stations with manually picked arrival-time data to ensure exact arrival times of *P* and *S* waves. A frequency range for computing t_0^* and $R(f)$ was selected above a threshold S/N ratio of 3. In cases where an available bandwidth above f_c was shorter than 5 Hz, the traces were skipped.

[21] Site-amplification factors may depend on the incident and azimuthal angles of rays propagating to stations, but for simplicity we assume that site-amplification factors depend only on frequencies. For stabilizing inversion procedures, stations with fewer than 20 observed earthquakes were not used in the analysis. In the inversion, we estimated t_0^* and $R(f)$ independently for *P* and *S* waves.

4.2.2. Corner Frequencies of *P* Waves

[22] As values of f_c estimated from S-coda waves are for *S* waves (f_{cs}), we need f_c for *P* waves (f_{cp}) for analyzing *P* wave spectral amplitudes. Ratios of *P* to *S* wave corner frequencies have been estimated to be 1.24–1.50 for small- to medium-

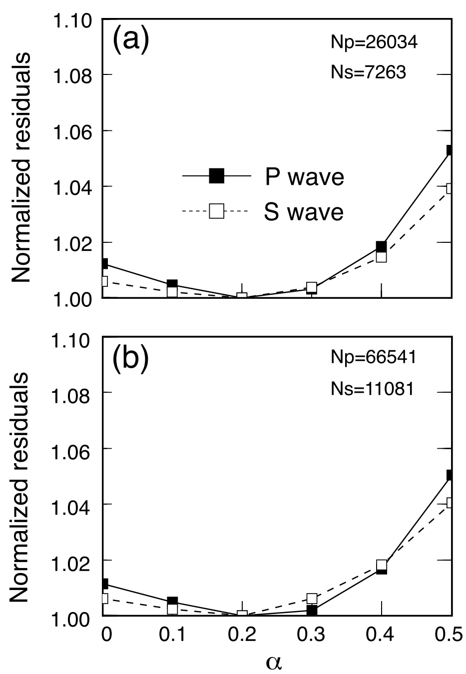

Figure 4. Normalized residuals of the misfit to spectra summed over all data, as a function of the frequency-dependent factor, α, for (a) shallow (H < 40 km) and (b) intermediate-depth (H ≥ 40 km) earthquakes. Black and white squares represent the results for *P* and *S* waves, respectively.

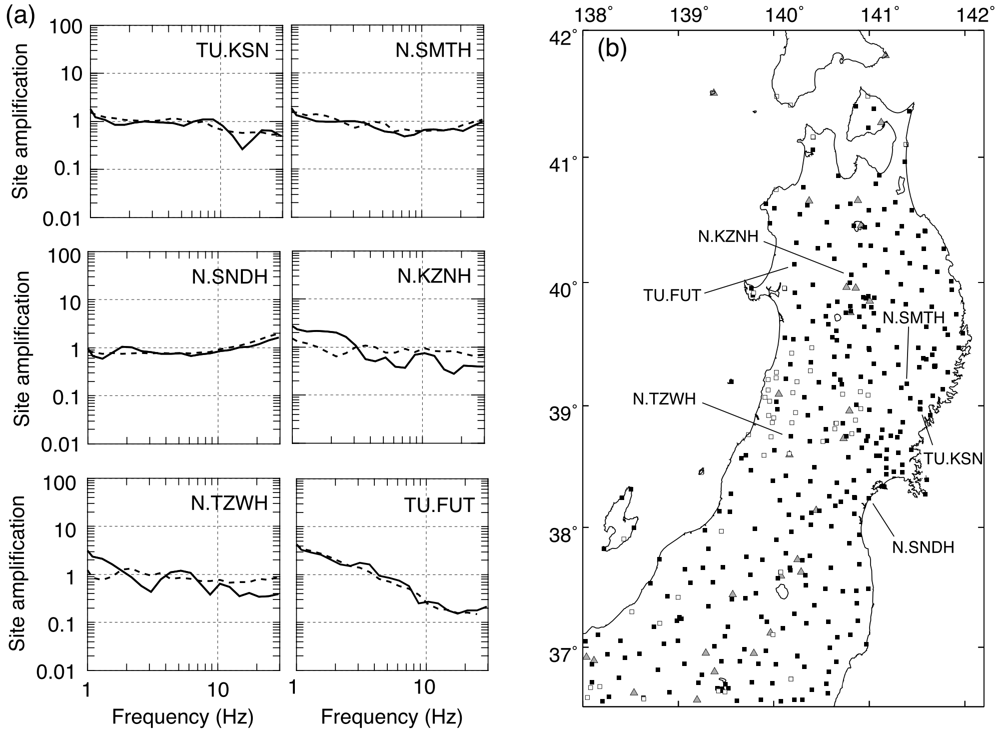

Figure 5. (a) Examples of relative site-amplification factors observed for *P* (solid lines) and *S* (dashed lines) waves at the six stations labeled in Figure 5b. (b) Distribution of all seismograph stations for which site-amplification factors were estimated. Stations with site-amplification factors for both *P* and *S* waves are shown by black squares, whereas those with site-amplification factors only for *P* waves are shown by white squares. Gray triangles denote active volcanoes.

sized earthquakes [e.g., *Boatwright et al*., 1991; *Stachnik et al*., 2004], and those observations are consistent with theoretically derived ratios of 1.2–1.5 [e.g., *Sato and Hirasawa*, 1973; *Madariaga*, 1976]. *Uchida et al*. [2007] analyzed *P* and *S* wave spectral amplitudes from 25 thrust-type earthquakes in NE Japan and found that f_{cp} is 1.33 times larger than f_{cs}. As the magnitude range of earthquakes ($2.5 \leq M \leq 4.8$) analyzed in *Uchida et al*. [2007] is almost the same as in this study, we calculated f_{cp} from the observed f_{cs} with the relationship $f_{cp} = 1.33 \times f_{cs}$.

4.2.3. Frequency Dependence of Q^{-1}

[23] Since α controls the decay rates of spectral amplitudes at higher frequencies, it is important to find an optimum value of α to establish a reliable attenuation model. We here find α that minimizes the residuals between the observed and theoretical spectral amplitudes for large data sets, following the method of *Stachnik et al*. [2004]. In the calculation, we set values of α from 0 to 1 with an increment of 0.1, and carried out inversions as described in section 4.1 for each value of α. The estimates were performed separately for shallow and intermediate-depth earthquakes to assess the differences in attenuation properties between the overlying crust and the mantle.

[24] For both shallow and intermediate earthquakes, the optimum value of α is estimated to be 0.2, but α of 0.1–0.3 also explains the data sets (Figure 4). The acceptable values of α for intermediate-depth earthquakes lie in a range of 0.1–0.5, which is observed for the mantle wedge in various subduction zones [*Flanagan and Wiens*, 1998; *Shito et al*., 2004; *Stackhnik et al*., 2004; *Takahashi*, 2012], and they are compatible with laboratory-derived values of solid olivine (0.2–0.4, with an optimum value of 0.27) [e.g., *Tan et al*., 1997; *Jackson et al*., 2002]. In contrast, α of 0.1–0.3 for shallow earthquakes overlaps with α of 0.1–0.5 observed in the crust of NE Japan [*Takahashi*, 2012] but is much smaller than α of 0.6–0.7 estimated for the crust in the Alaska subduction zone [*Stachnik et al*., 2004]. Although this inconsistency may be attributable to differences in the nature of crustal rocks in terms of temperatures, fluid contents, and chemical compositions, we cannot quantify this discrepancy because of the lack of systematic experiments on the effect of crustal materials on seismic attenuation.

[25] The best fit value (α = 0.2) for shallow and intermediate-depth earthquakes is close to the optimum value (α = 0.27), which is derived from laboratory experiments for high-temperature mantle rocks [e.g., *Jackson et al*., 2002; *Karato*, 2003]. These experiments are probably most relevant to the mantle wedge, so we adopted α of 0.27 as the frequency-dependent factor in this study.

4.3. Results

4.3.1. Site-Amplification Factors

[26] We obtained relative site-amplification factors for 371 and 318 stations for *P* and *S* waves, respectively. Examples of site-amplification factors estimated for six stations are shown in Figure 5. Site-amplification factors for *P* waves are similar to those for *S* waves at stations N.SMTH, N.SNDH, and TU.FUT, but are different from those for *S* waves at other stations. For *P* waves, site-amplification factors at stations N.KZNH, N.TZWH, and TU.FUT show

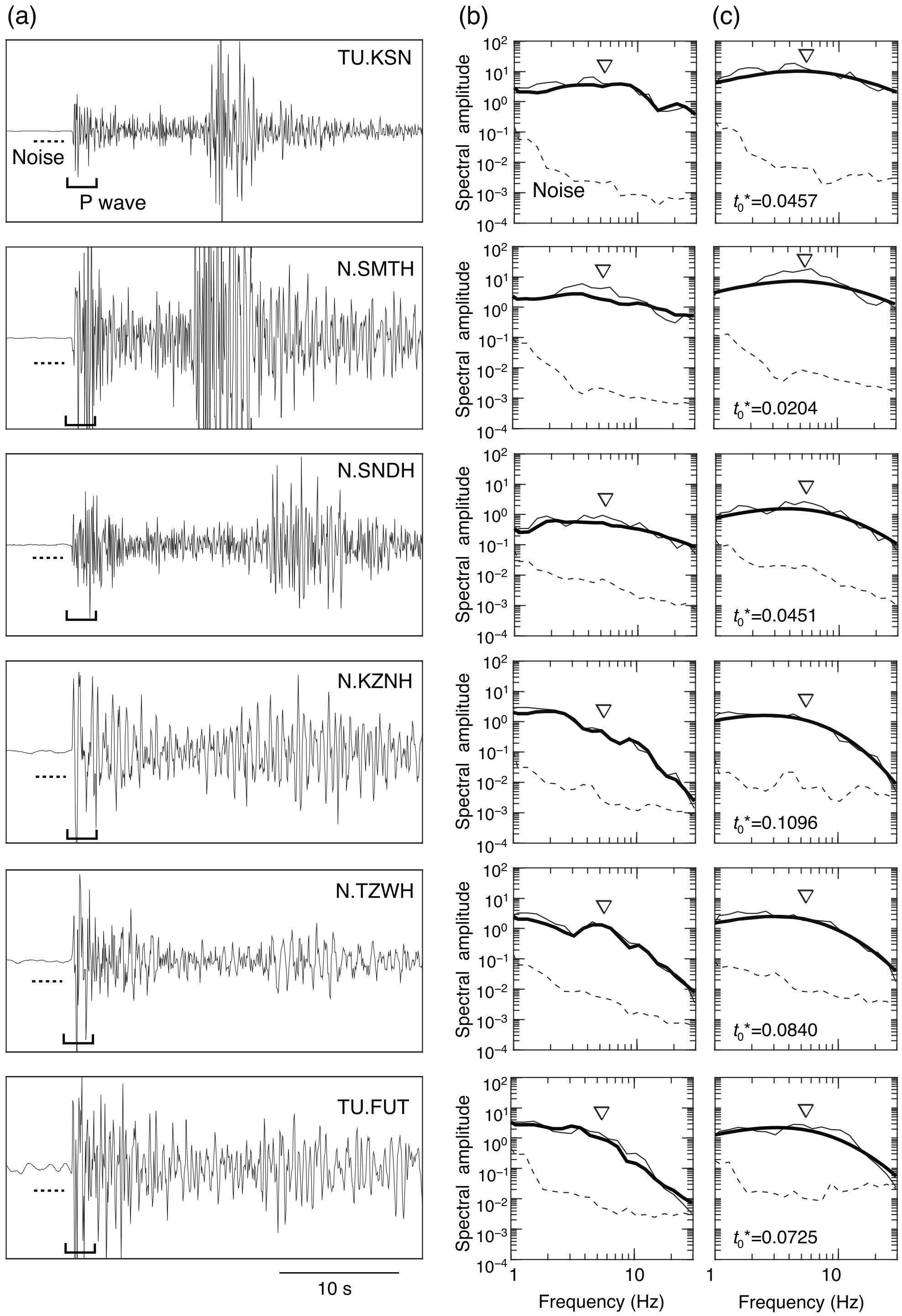

Figure 6. Examples of estimates t_0^* of for P waves from an intermediate-depth earthquake recorded at six stations for which the site-amplification factors are shown in Figure 5. (a) Velocity waveforms in the vertical component for a time window of 35 s including P and S waves. Names of stations are shown in the upper-right-hand corner. Time windows with a length of 2.56 s for P waves and noises are shown by brackets and dashed lines, respectively. (b) Spectral amplitudes observed for P waves (thin lines) and noises (dashed lines). Inverted triangles denote the corner frequency of the earthquake ($f_{cp} = 5.5$ Hz). The thick line represents the theoretical amplitude spectrum calculated from the optimum value of t_0^*, site-amplification factors, and the ω^2 source model. (c) Spectral amplitudes for P waves and noises corrected for site-amplification factors. The thick line represents the theoretical amplitude spectrum calculated from the optimum value of t_0^* and the ω^2 source model. Values of t_0^* are shown. Symbols are the same as in Figure 6b.

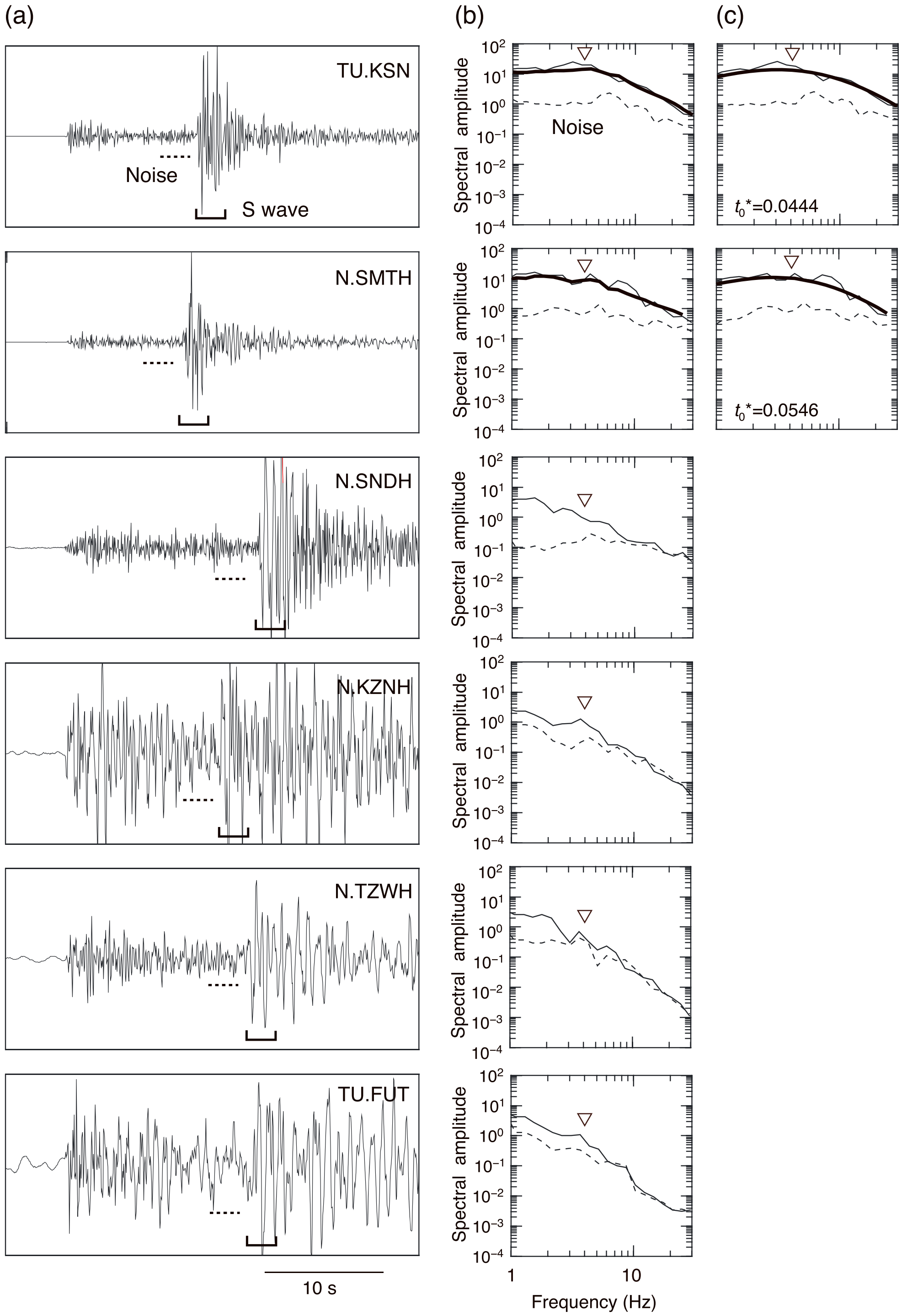

Figure 7. Examples of the estimates of t_0^* for *S* waves from the intermediate-depth earthquake shown in Figure 6. (a) Velocity waveforms in the transverse component for a time window of 35 s including *P* and *S* waves. Time windows with a length of 2.56 s for *S* waves and noises are shown by brackets and dashed lines, respectively. (b) Spectral amplitudes observed for *S* waves (thin lines) and noises (dashed lines). Inverted triangles denote the corner frequency of the earthquake ($f_{cs} = 4.1$ Hz). Theoretical spectra cannot be estimated at stations N.SNDH, N.KZNH, N.TZWH, and TU.FUT because of unfavorable S/N ratios at high frequencies. (c) Spectral amplitudes for *S* waves and noises corrected for site-amplification factors at stations TU.KSN and N.SMTH. Symbols are the same as in Figure 7b.

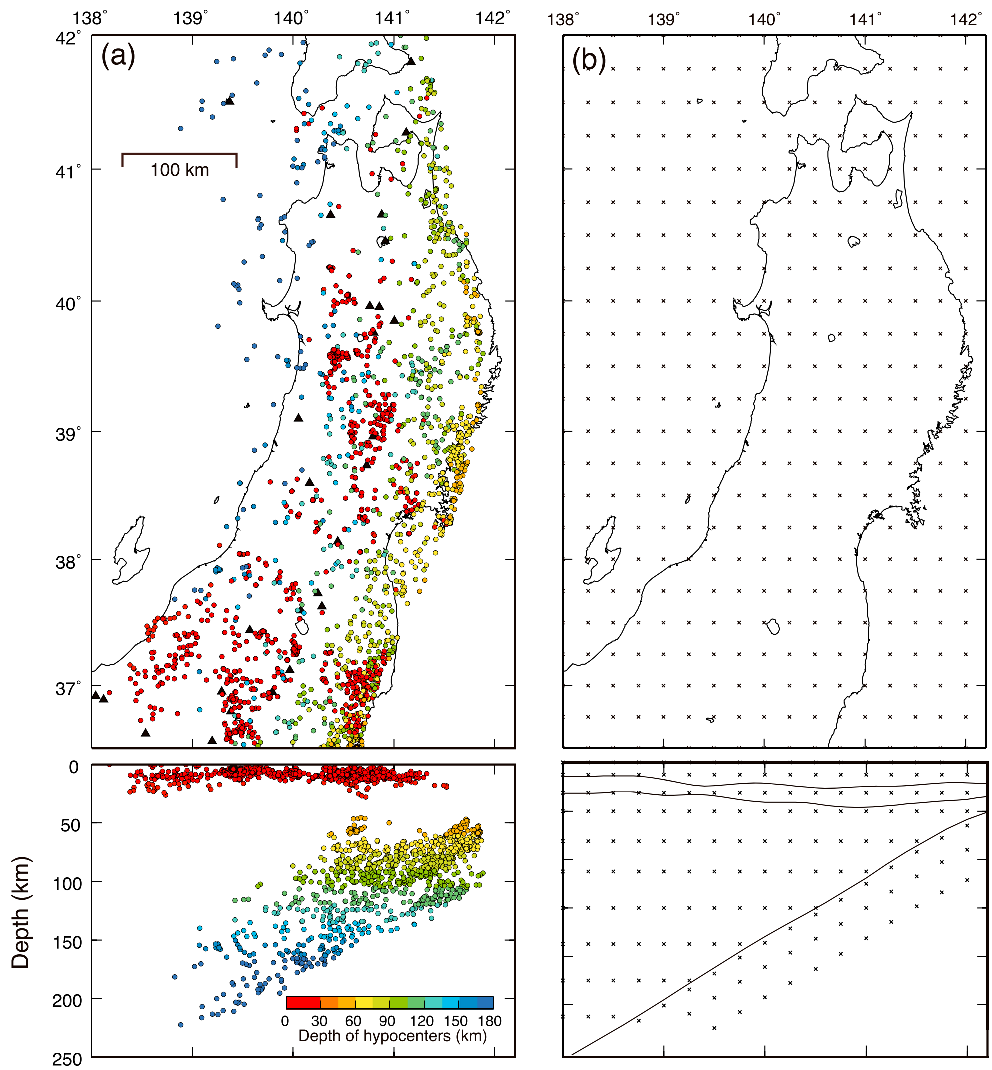

Figure 8. (a) Distribution of earthquakes used in the tomographic inversion. Colors represent the focal depths. Black triangles denote active volcanoes. (b) Map and cross-sectional views of configurations of grid nodes (crosses) adopted in the inversion. Solid lines denote the Conrad and Moho [*Katsumata*, 2010], and the upper interface of the Pacific plate [*Nakajima et al.*, 2009].

systematic frequency dependencies, with amplification at low frequencies and de-amplification at high frequencies, together with local peaks and troughs. In contrast, stations N.SNDH and N.SMTH show more stable site-amplification factors with small fluctuations.

[27] Station N.SNDH is a deep borehole station (1206 m below the sea level) and is installed in indurated Triassic sandstone. *Takahashi et al.* [2005] selected this station as a reference station and successfully derived site-amplification factors for stations in NE Japan. As shown in Figure 5a, site-amplification factors at station N.SNDH depend little on frequency for both *P* and *S* waves, and amplification factors range from 0.7 to 2.0. These results indicate that site-amplification factors are estimated appropriately by the joint inversion with t_0^*.

4.3.2. Values of t^*

[28] Figure 6 presents examples of velocity waveforms and *P* wave spectral amplitudes observed for an earthquake that occurred at a depth of 93 km beneath the volcanic front. High-frequency components are less prominent in waveforms observed at stations located in the back-arc side (N.KZNH, N.TZWH, and TU.FUT) than those in the fore-arc side (TU.KSN, N.SMTH, and N.SNDH). The stations located in the back arc show a marked decay in spectral amplitudes above $>\sim$10 Hz, whereas the stations in the fore arc have large spectral amplitudes even at high frequencies (thin lines in Figure 6b).

[29] Theoretical spectral amplitudes calculated from the estimated t_0^*, site-amplification factors, and the ω^2 source model fit very well to the observed spectra and reproduce small peaks and troughs (thick lines in Figure 6b). After the corrections for site-amplification factors, the observed spectra show a smooth pattern over the frequency range of interest (thin lines in Figure 6c), and are explained by the calculated t_0^* together with the ω^2 source model (thick lines in Figure 6c). Comparisons of spectral amplitudes with and

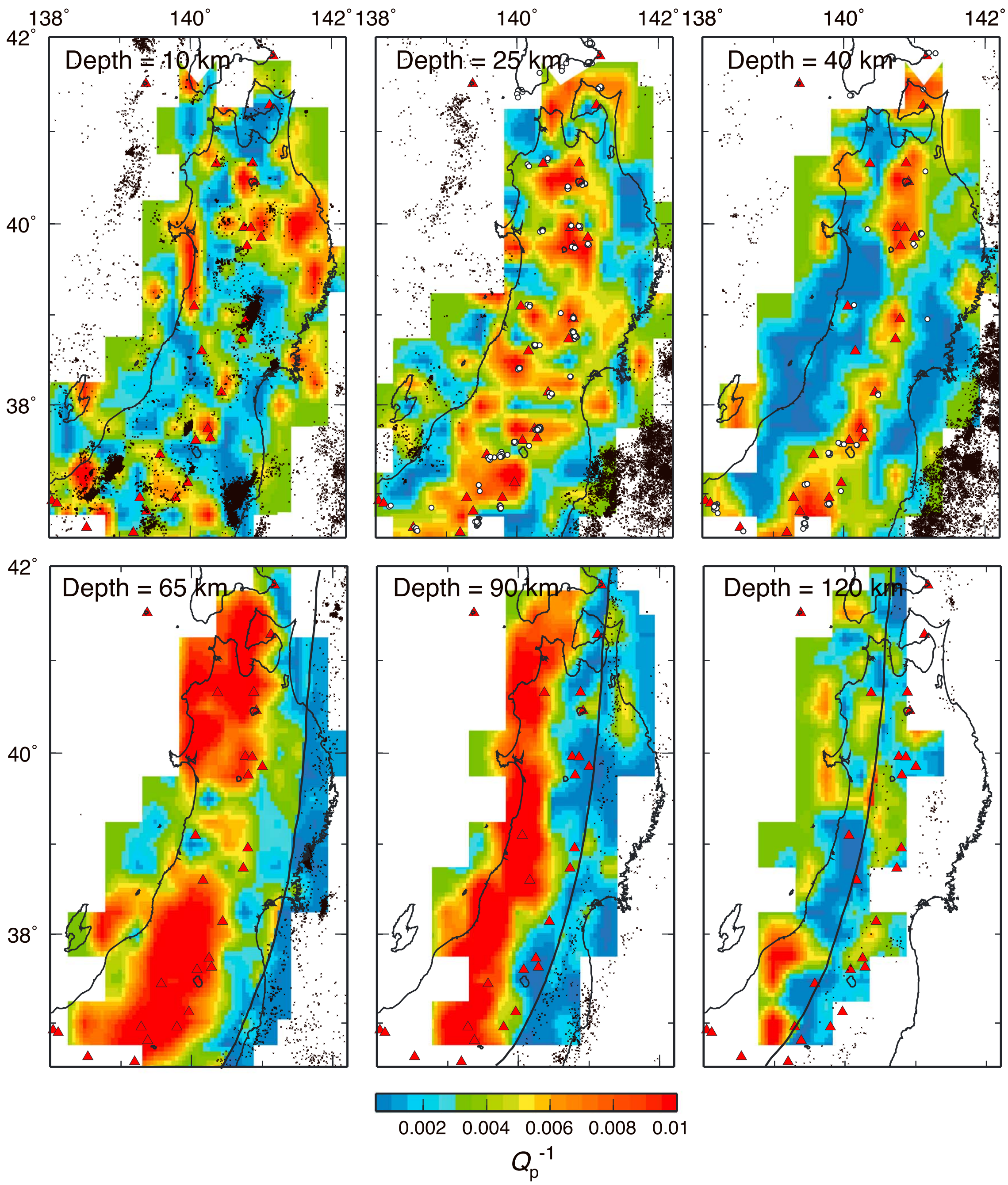

Figure 9. Map showing $Q_p{}^{-1}$ obtained in this study at depths of 10, 25, 40, 65, 90, and 120 km. The color scale for $Q_p{}^{-1}$ is shown at the bottom. Red triangles represent active volcanoes. Black dots and white circles represent ordinary earthquakes and deep low-frequency earthquakes, respectively, that occurred within 5 km from each depth slice. Only the regions with good recovery for checkerboard resolution tests are shown. The Pacific plate lies to the right of black curves at depths of 65–120 km.

without the corrections for site-amplification factors suggest that site-amplification factors with a strong frequency dependence, such as at stations N.KZNH, N.TZWH, and TU.FUT, introduce systematic biases in the estimates of t_0^*. Without the corrections for site-amplification factors, we would estimate higher values of t_0^* for these stations, because observed spectra are significantly amplified at low frequencies and deamplified at high frequencies. These results suggest the importance of the estimates of site-amplification factors to determine reliable values of t_0^*.

[30] Figure 7 shows examples of velocity waveforms and *S* wave spectral amplitudes observed for the same earthquake-station pairs presented in Figure 6. Except for stations TU. KSN and N.SMTH, high-frequency components in *S* waves are very weak and the S/N ratios become smaller than the threshold of 3 above frequencies of 5–10 Hz (Figure 7b).

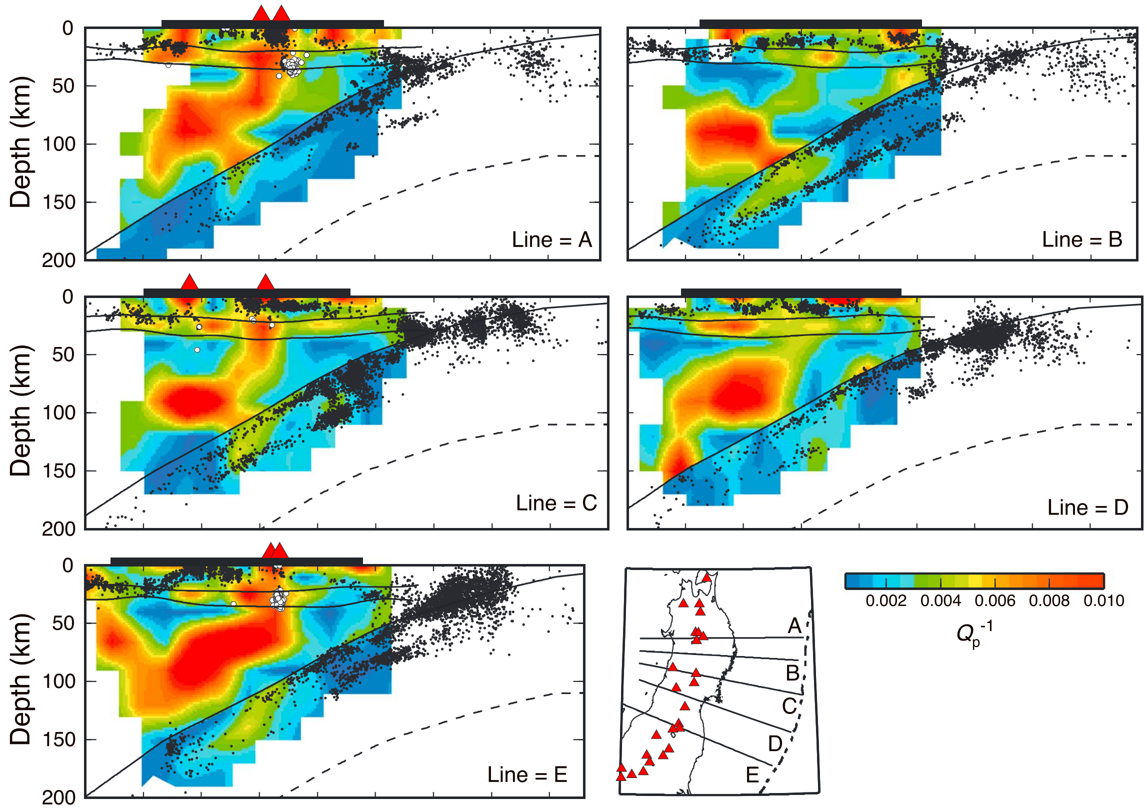

Figure 10. Across-arc vertical cross sections of Q_p^{-1} along five profiles shown in the inset map. Solid lines indicate the Conrad and Moho, and the upper surface of the Pacific plate adopted in the tomographic inversion. Black bars on the top of each panel denote the land area. Black dots and white circles represent ordinary earthquakes and deep low-frequency earthquakes, respectively, that occurred within 10 km from each profile. Only the regions with good recovery for checkerboard resolution tests are shown. Other symbols are the same as in Figure 9.

Because of the low S/N ratios at high frequencies and the resulting narrow range of frequencies available above f_c, we cannot estimate reliable values of t_0^* for *S* waves at stations N.SNDH, N.KZNH, N.TZWH, and TU.FUT. For many source-receiver pairs whose raypaths propagate mainly in the back-arc mantle wedge, values of t_0^* for *S* waves cannot be determined because of the low S/N ratios at high frequencies. This creates a dilemma whereby we cannot estimate reliable *S* wave attenuation structure (Q_s^{-1}) in the back-arc mantle wedge in spite of the presence of a medium that strongly attenuates *S* waves. Therefore, this study estimates only 3-D *P* wave attenuation structure in the crust and upper mantle beneath NE Japan. Estimates of Q_s^{-1} will be a subject of future studies.

5. Tomographic Inversions

5.1. Data and Method

[31] We estimate 3-D Q_p^{-1} structure by the inversion of t_0^* [e.g., *Rietbrock*, 2001]. Hypocenters of earthquakes used in the inversion are shown in Figure 8a. We employed the ray-tracing technique of *Zhao et al.* [1992] to calculate raypaths and travel times for the 3-D *P* wave velocity model by *Nakajima et al.* [2001]. The Conrad and Moho in the overlying plate [*Katsumata*, 2010] and the upper boundary of the subducting Pacific plate [*Nakajima et al.*, 2009] were introduced as velocity discontinuities in the model space (Figure 8b).

[32] For the model space, we considered a latitude range of 36.5°N–42°N, a longitude range of 138°E–142.5°E, and a depth range of 0–210 km. Two 3-D grid nets were set in the model space, and a value of Q_p^{-1} for each grid node was estimated. One net covered the crust and mantle wedge in the overlying plate with grids spaced at an interval of 0.25° in the horizontal direction and intervals of 10–25 km in the vertical direction (Figure 8b), and the other net covered in the subducting Pacific slab. In the slab, we set grid nodes subparallel to the slab surface with distances of 5, 25, and 50 km from the slab surface. We set initial values of Q_p^{-1} to be 0.003 for grid nodes in the crust and mantle wedge, and 0.001 for grid nodes in the Pacific slab.

[33] The total number of t_0^* values used in the inversion was 105,264. We estimated Q_p^{-1} values at grid nodes with more than 100 rays. The optimum damping parameter was chosen to be 50 based on the trade-off curves between model variances and data residuals [e.g., *Eberhart-Phillips*, 1986] (Figure S1 in auxiliary materials). The final results were obtained after five iterations. The RMS of t_0^* residuals was reduced from 0.035 s in the initial model to 0.018 s upon optimization.

[34] We conducted three synthetic tests to assess the resolution of the obtained attenuation structure. The results of the three synthetic tests demonstrated that the data set can resolve the 3-D attenuation structure with spatial resolutions of 20–25 km in both the horizontal and vertical directions. The obtained Q_p^{-1} structure is reliable within errors of ~10% for high-attenuation areas and of 20–30% for low-attenuation areas (details of the resolution tests are presented in auxiliary materials with Figures S2–S4).

5.2. Results

[35] This study considers α of 0.27, and Q_p^{-1} values estimated in this study correspond to those at 1 Hz. With α of 0.27, values of Q_p^{-1} at 5 and 10 Hz are 64% and 53% of Q_p^{-1} at 1 Hz, respectively.

[36] Figure 9 shows a map of the obtained Q_p^{-1} at depths of 10, 25, 40, 65, 90, and 120 km. At a depth of 10 km (the upper crust), high-attenuation areas are distributed in the northern part of the fore-arc side, around active volcanoes, and along some parts of the Japan Sea coastline. Seismic activity appears to be high in areas where seismic attenuation is relatively low. In the lower crust at a depth of 25 km, Q_p^{-1} is locally high beneath volcanic clusters striking transverse to the arc. These features are consistent with the distribution of *S* wave attenuation estimated from maximal amplitudes of *S* waves [*Takahashi*, 2012] and from S-coda waves [*Carcole and Sato*, 2009]. Deep, low-frequency earthquakes [e.g., *Hasegawa and Yamamoto*, 1994] are distributed in or near areas of marked high attenuation.

[37] A high-attenuation zone is continuously distributed along the volcanic front at a depth of 40 km, which corresponds spatially with a zone of low seismic velocity [e.g., *Nakajima et al.*, 2001; *Zhao et al.*, 2012]. The back-arc mantle wedge as a whole shows high attenuation ($Q_p^{-1} > 0.005$) at depths of 65 and 90 km, but an area with low to moderate attenuation ($0.002 < Q_p^{-1} < 0.005$) is observed in the back-arc side at a depth of 65 km. The uppermost mantle with low to moderate attenuation in the latitude range of 39°N–40°N was also suggested by *Matsuzawa et al.* [1989] and *Takahashi* [2012]. In the subducting Pacific slab, seismic attenuation is essentially low, but some parts show moderate to slightly high attenuation.

[38] The across-arc variation in seismic attenuation in the mantle wedge is represented clearly in across-arc vertical cross sections (Figure 10). Attenuation structure changes abruptly between the fore-arc and back-arc sides, with high attenuation in the back arc and low attenuation in the fore arc. We observe an inclined high-attenuation zone with $Q_p^{-1} > 0.005$ in the back-arc mantle wedge, which extends from the back arc at a depth of ~100 km to the crust beneath the volcanic front. The inclined high-attenuation zone appears to be maturely developed in cross sections that intersect active volcanoes (lines A, C, and E in Figure 10). The inclined high-attenuation zone corresponds spatially with the inclined low-velocity zone interpreted as the upwelling flow (Figure 1b), suggesting that upwelling flow shows high attenuation as well as low velocity. An interesting feature is the existence of a high-attenuation area that spreads out from the slab interface to the mantle wedge at a depth of ~120 km (lines A–D).

[39] To quantify the 1-D depth variation in seismic attenuation, we calculated the average attenuation and its standard deviation at depths of 40, 65, 90, and 120 km. The average attenuation at depths of 40 and 65 km was calculated separately for the fore-arc and back-arc sides. Although the standard deviation of attenuation at each depth is relatively large, attenuation in the back-arc mantle (red squares in Figure 11) shows a marked variation with depth. Attenuation in the back-arc mantle is low at a depth of 40 km, highest at a depth of 65 km, and becomes lower with increasing depth. Attenuation in the fore-arc mantle (blue squares in Figure 11) has almost the same value (~0.003) at depths of 40 and 65 km.

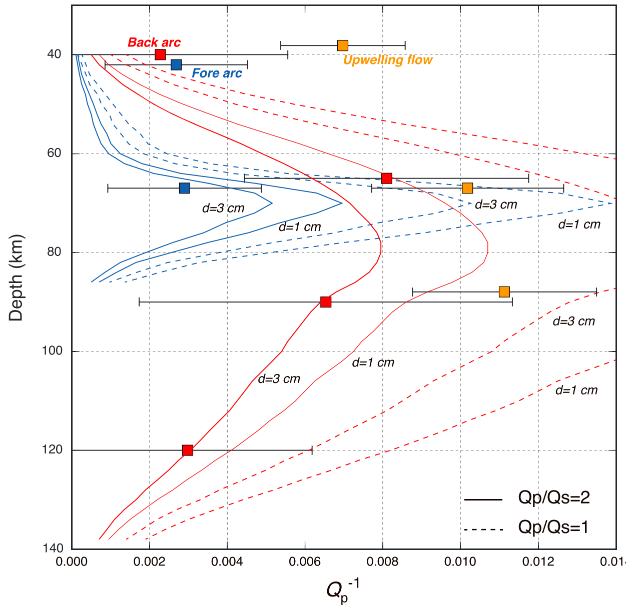

Figure 11. Depth profile of Q_p^{-1}. Red squares denote the average value of Q_p^{-1} observed in the back-arc mantle at depths of 40, 65, 90, and 120 km, whereas blue squares denote the average value of Q_p^{-1} in the fore-arc mantle at depths of 40 and 65 km. Orange squares denote the average values of Q_p^{-1} observed in the inclined high-attenuation zone at depths of 40, 65, and 90 km, which are calculated from attenuation model shown in Figure 12a. Horizontal bars represent the standard deviation of each value. Red and blue curves denote the theoretical depth profiles of Q_p^{-1} in the back-arc and fore-arc mantle, respectively, calculated with equation (9) and the 2-D thermal model shown in Figure S5a in auxiliary materials. Grain sizes (*d*) of 1 and 3 cm and Q_p/Q_s values of 1 and 2 are assumed in the calculation.

6. Discussion

6.1. Factors Controlling Seismic Attenuation in the Mantle

[40] Seismic attenuation in the upper mantle depends on many factors, such as temperature, grain size, H_2O content, compositional variation, and the existence of melt. Among these factors, a small variation in major element chemistry is likely to have little effect on anelasticity [*Karato*, 2003]. In contrast, temperature variation [e.g., *Faul and Jackson*, 2005] and grain size distribution [e.g., *Jackson et al.*, 2002] are considered to have a dominant effect on attenuation. The existence of hydrous phases and melt potentially

enhances attenuation in the seismic frequency band, but experimental studies do not still provide a means for quantitatively evaluating the effects of hydrous phases and melt on attenuation [e.g., *Gribb and Cooper*, 2000; *Jackson et al.*, 2004; *Aizawa et al.*, 2008; *McCarthy and Takei*, 2011].

[41] Laboratory measurements have yielded experimental relationships for melt-free polycrystalline olivine between Q_s^{-1} and temperature, pressure, frequency, grain size, and C_{OH} content [e.g., *Jackson et al.*, 2002; *Faul and Jackson*, 2005; *Behn et al.*, 2009]. An experimentally derived equation for Q_s^{-1} proposed by *Behn et al.* [2009] is expressed as follows:

$$Q_s^{-1}(f, T, P, C_{OH}, d) = \left[Bd^{-P_q}(2\pi f)^{-1}\exp\left(-\frac{E+PV}{RT}\right)\right]^{\alpha} \quad (9)$$

where B is a pre-exponential factor calculated for a C_{OH} of 1000 H/10^6 Si, d is the grain size, P_q is the grain-size exponent, f is frequency, E and V are activation enthalpy and volume, respectively, P is pressure, R is the gas constant, T is absolute temperature, and α is a frequency-dependent factor.

6.2. Temperature and Grain Size in the Mantle Wedge

[42] We calculated a temperature field beneath NE Japan using a 2-D time-dependent thermal and mantle-flow model, following *Torii and Yoshioka* [2007] and *Yoshioka et al.* [2008]. In the calculation, we considered the geometry of the subducting Pacific plate [*Nakajima et al.*, 2009] and assumed the age of the Pacific plate to be 127 Ma with a subduction rate of 8.4 cm/yr. We set a maximum decoupling depth of 66 km for the fore-arc mantle wedge to become stagnant. The 2-D temperature field thus modeled for NE Japan is shown in Figure S5 in auxiliary materials.

[43] We calculated 1-D temperature profiles for the fore-arc and back-arc mantle wedges by averaging the 2-D temperature field (Figure S5). For the 1-D temperature profile, we calculated Q_s^{-1} with equation (9). In the calculations, we assumed constant grain sizes of 1 and 3 cm [e.g., *Rychert et al.*, 2008; *Wada et al.*, 2011] and used the same values for other parameters as given in *Wada et al.* [2011]. Because values of Q_p/Q_s in the mantle wedge have been constrained with a range from 1.0 to 2.15 [e.g., *Roth et al.*, 1999; *Shito and Shibutani*, 2003; *Stachnik et al.*, 2004; *Pozgay et al.*, 2009], we assumed Q_p/Q_s of 1 and 2 as end-members to convert the calculated Q_s^{-1} to Q_p^{-1}.

[44] A depth profile of Q_p^{-1} expected for the 1-D temperature profile is presented in Figure 11. The pattern of Q_p^{-1} observed in the back-arc mantle can be explained by the depth variation in Q_p^{-1} calculated with $Q_p/Q_s = 2$ and grain sizes of 1 or 3 cm (red curves in Figure 11), even though the observed Q_p^{-1} at a depth of 40 km is slightly higher than the calculated value. These results indicate that Q_p^{-1} in the back-arc mantle wedge is controlled primary by thermally activated processes such as grain boundary sliding and the motion of defects and dislocations [e.g., *Jackson et al.*, 2002]. Q_p^{-1} calculated with $Q_p/Q_s = 1$ (red broken curves in Figure 11) is much higher than the observed values, suggesting that Q_p/Q_s values in the mantle wedge are much greater than ~1.

[45] The observed Q_p^{-1} in the fore arc at a depth of 65 km is compatible with the Q_p^{-1} calculated with a grain size of 3 cm and $Q_p/Q_s = 2$. However, there is a large inconsistency between the calculated and observed Q_p^{-1} at a depth of 40 km, where the average temperature is estimated to be 780°C in the 2-D thermal modeling. Since this temperature lies within the range of temperature estimates (600–880°C) derived from heat flow and seismic velocity data [e.g., *Sato*, 1992], the temperature estimates are probably relevant. The identified inconsistency is probably due to the presence of somewhat-isolated high-attenuation areas ($Q_p^{-1} > \sim 0.005$) in the fore-arc mantle (Figure 9), which result in an apparent increase in the average attenuation. Except for these high-attenuation areas where fluids may be present, the overall attenuation is as low as ~0.001, and this value can be explained by Q_p^{-1} expected for the thermal model. An inappropriate application of equation (9) to a low-temperature condition (~780°C) may also yield additional, substantial uncertainties in the calculation of attenuation.

6.3. Cause of an Inclined High-Attenuation Zone

[46] To quantify the origin of the upwelling flow, we calculated the average Q_p^{-1} for the inclined high-attenuation zone at depths of 40, 65, and 90 km (orange squares in Figure 11). Although the observed Q_p^{-1} at depths of 65 and 90 km is comparable to Q_p^{-1} calculated with a grain size of 1 cm and Q_p/Q_s of 2, the calculated Q_p^{-1} does not account for the observed Q_p^{-1} of ~0.007 at a depth of 40 km, regardless of grain sizes and Q_p/Q_s ratios. A temperature as high as 1250°C can reproduce the observed Q_p^{-1} at a depth of 40 km, but areas with such a high temperature are not apparent from seismological observations [e.g., *Takanami et al.*, 2000; *Nakajima and Hasegawa*, 2003] and from heat flow data [e.g., *Sato*, 1992]. These comparisons suggest that factors other than high temperature are required for the further enhancement of attenuation in the upwelling flow.

[47] *Nakajima et al.* [2005] analyzed velocity reduction rates in the inclined low-velocity zone and estimated melt volume fractions of 3–6 vol% at a depth of 90 km, 0.04–0.05 vol% at a depth of 65 km, and 1–2 vol% at a depth of 40 km. *Takei and Holtzman* [2009] suggested that even a small amount of melt can result in high attenuation if the effect of melt on anelasticity is not negligible. Therefore, the enhancement of attenuation in the upwelling flow is probably associated with the existence of partial melt. Although the effect of melt on attenuation still holds a large amount of uncertainty for quantitative analysis, a consequence of our interpretation implies that partial melt contributes to the enhancement of attenuation in the seismic frequency band [e.g., *Jackson et al.*, 2004]

6.4. Implications for Arc Magmatism

[48] Seismic attenuation in the mantle upwelling flow does not vary a lot along the arc (Figure 12a), in contrast to seismic velocity that shows a marked along-arc variation with spatial correlations with Quaternary volcanoes and deep, low-frequency earthquakes (Figure 12b). Since seismic attenuation is controlled primarily by temperature and seismic velocity is much more sensitive to variations in the degree of partial melt [e.g., *Nakajima et al.*, 2005], these observations suggest that the degree of partial melt varies significantly along the arc, forming wet fingers in the upwelling flow. This implies that along-arc variations in surface and subsurface magmatic manifestations are not

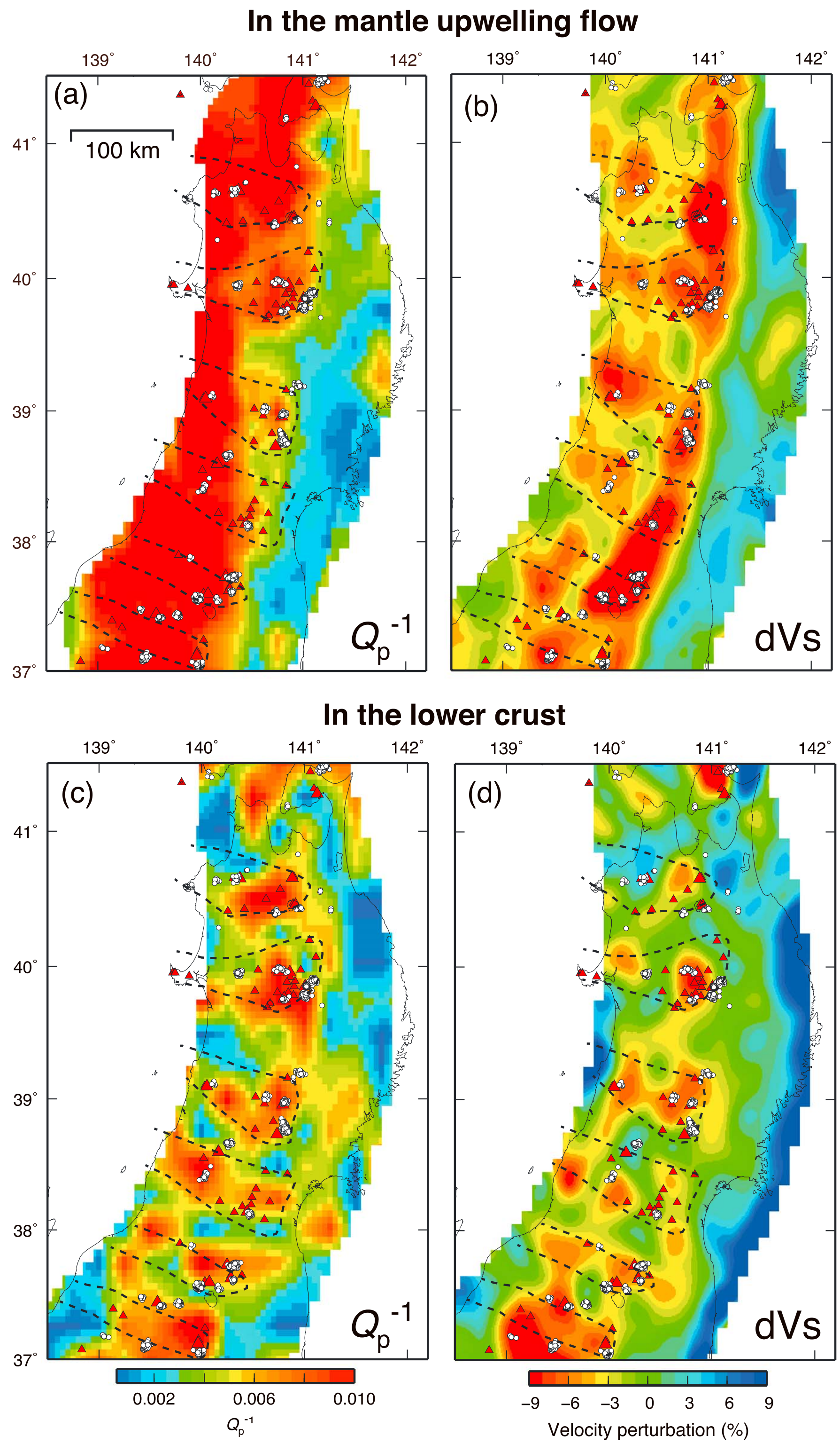

Figure 12. Map showing of (a) Q_p^{-1} and (b) S wave velocity perturbation (%) along the mantle upwelling flow and (c) Q_p^{-1} and (d) S wave velocity perturbation (%) in the lower crust in the overlying plate. The attenuation and velocity scales are shown at the bottom of each diagram. Large and small red triangles denote active and Quaternary volcanoes, respectively. White circles represent deep, low-frequency earthquakes that occurred around the Moho. Black dashed lines indicate clustering of volcanoes striking transverse to the arc [*Tamura et al.*, 2002]. In Figure 12a, the highest values of Q_p^{-1} along the inclined high-attenuation zone are plotted as a map for the back-arc mantle, whereas Q_p^{-1} at a depth of 40 km is plotted for the fore-arc mantle. The calculation of the highest Q_p^{-1} in the back-arc mantle is limited to areas with a distance range of 20–70 km above the slab interface. S wave velocity model is taken from *Hasegawa and Nakajima* [2004].

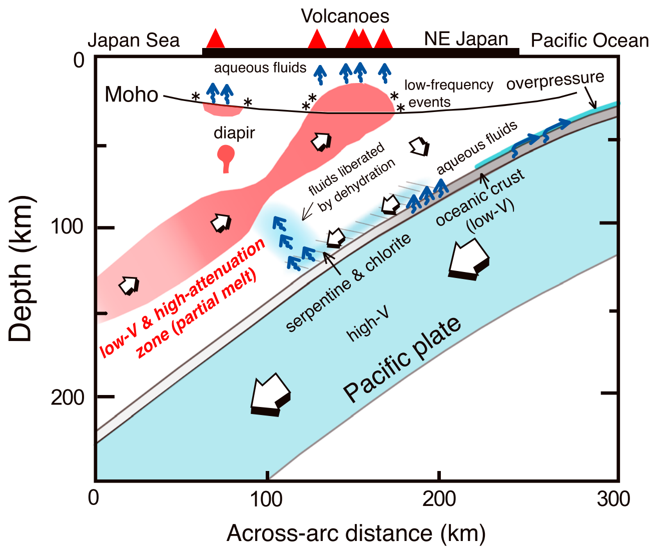

Figure 13. A schematic cartoon of across-arc vertical cross section showing the transportation paths of fluids and melts beneath NE Japan, which is modified from *Hasegawa and Nakajima* [2004] and *Hasegawa et al*. [2013].

caused by thermal variations in the mantle wedge associated with hot fingers [*Tamura et al*., 2002] or with small-scale convection [*Honda and Yoshida*, 2005]. The along-arc variations in the degree of partial melt may result from the gravitational instability of buoyant fluids that are supplied to the upwelling flow from the underlying Pacific slab.

[49] The partial melt is conveyed through the upwelling flow and is accumulated beneath the Moho due to the density contrast, resulting in 1–2 vol% melts as dikes or cracks [*Nakajima et al*., 2005]. The melt accumulated beneath the Moho is represented as a high-attenuation and low-velocity zone along the volcanic front at a depth of 40 km (Figure 9). The melt then migrates upward in the lower crust because of its buoyancy, where fractional crystallization and chemical reactions with the surrounding crustal rocks can occur. This interpretation indicates that the location of the volcanic front is controlled by the geometry of the inclined upwelling flow resulting from the tectonic architecture.

[50] The clustering of Quaternary volcanoes corresponds spatially to high-attenuation and low-velocity zones in the lower crust (areas enclosed by broken lines in Figures 12c and 12d). This correlation is an important observation in terms of magmatism in the back-arc side, because the main stream of the upwelling flow does not convey a large amount of partial melt toward the back-arc side (Figure 10). A likely mechanism that supplies melt efficiently to the back-arc lower crust is the sporadic segregation of partial melt from the upwelling flow as diapirs (Figure 13), raising the melt vertically in the overlying mantle wedge due to buoyancy. Repeated intrusions of melt into the lower crust that have taken place during the Quaternary facilitate volcanism in the back-arc side. It is noted that the absence of spatial correlation between the clustering of Quaternary volcanoes and high-attenuation zones in the upper crust (Figure 9) suggests that the upper crust does not store a large amount of melt that can be detected by seismic tomography with spatial resolutions of 20–25 km.

6.5. Path of Fluids From the Pacific Slab

[51] Our results give a clue to understand the liberation of aqueous fluids from a hydrous layer above the Pacific slab. *Iwamori* [1998] suggested that a thin hydrous layer is formed immediately above the interface of subducting slab and dehydration of hydrous minerals in that layer occurs at depths of 150–200 km for cold subduction zones like NE Japan. However, recent seismological observations beneath NE Japan have shown the presence of a hydrous layer immediately above the slab only down to depth of 110–130 km [*Kawakatsu and Watada*, 2007; *Tsuji et al*., 2008], which is much shallower than the depth predicted by *Iwamori* [1998].

[52] We revealed the existence of a high-attenuation area that spreads out from the slab interface to the mantle wedge at a depth of ~120 km (lines A–D in Figure 10). Interestingly, the depth of 120 km is consistent with the depth of the downdip end of the hydrous layer observed above the plate interface [*Kawakatsu and Watada*, 2007; *Tsuji et al*., 2008]. Our observations suggest that the breakdown of hydrous minerals hosted in the hydrous layer above the plate interface occurs at a depth of ~120 km and that large amounts of fluids are released to the mantle wedge as schematically shown in Figure 13, resulting in high attenuation areas immediately above the plate interface. A deflection of fluids toward the back arc from their buoyant vertical migration path, as observed in this study, is predicted from numerical simulations of solid mantle flow incorporating buoyancy-drive fluid migration [e.g., *Cagnioncle et al*., 2007].

7. Conclusions

[53] We estimated 3-D Q_p^{-1} structure beneath NE Japan by analyzing seismograms observed at a nation-wide seismograph network in Japan, and discussed the obtained Q_p^{-1} structure in terms of mantle dynamics and arc magmatism. Our observations have provided crucial constraints on ongoing mantle-wedge process beneath the NE Japan arc. The main conclusions are as follows.

[54] 1. We estimated the corner frequencies of earthquakes from spectral ratios of S-coda waves, and then performed a joint inversion to simultaneously determine attenuation terms and frequency-dependent site-amplification factors. This strategy can minimize the trade-off among unknown parameters in the analysis.

[55] 2. The depth dependence of Q_p^{-1} observed in the back-arc mantle can be explained by Q_p^{-1} calculated from the 2-D thermal model with a Q_p/Q_s value of 2 and grain sizes of 1–3 cm.

[56] 3. An inclined high-attenuation zone is observed in the back-arc mantle, which corresponds to the mantle upwelling flow formerly identified as a low-velocity zone. Since attenuation in the upwelling flow is higher than that expected for the 2-D thermal structure, attenuation is probably enhanced by the presence of partial melt in the flow.

[57] 4. The upwelling flow shows a marked along-arc variation in seismic velocity but not in seismic attenuation. This observation suggests that surface and subsurface magmatism is controlled by the along-arc variations in the degree of partial melt rather than in temperature distribution.

[58] 5. A high-attenuation area that spreads out from the slab interface to the mantle wedge is observed at a depth of ~120 km. The high attenuation is probably caused by the

breakdown of hydrous minerals hosted in the hydrous layer above the plate interface.

[59] An important topic for future research is to estimate seismic attenuation for *S* waves. Precise estimates of attenuation ratios between *P* and *S* waves, as well as laboratory experiments on the influences of melt and free water on seismic attenuation, will enhance our understanding of mantle-wedge processes associated with the subduction of hydrous minerals and the resulting dehydration reactions in subduction zones.

[60] **Acknowledgments.** We thank Y. Takei, T. Takahashi, and T. Maeda for comments and discussions. Constructive and careful reviews by two anonymous reviewers improved the manuscript. We used seismic data recorded at a nationwide seismograph network. All the figures in this paper were plotted using GMT [*Wessel and Smith*, 1998]. This work was supported by the Ministry of Education, Culture, Sports, Science, and Technology of Japan, under its Observation and Research Program for the Prediction of Earthquakes and Volcanic Eruptions, and by JSPS KAKENHI Grant Number 24740300.

References

Aizawa, Y., A. Barnhoorn, U. H. Faul, J. D. Fitz Gerald, I. Jackson, and I. Kovacs (2008), Seismic properties of Anita Bay dunite: An exploratory study of the influence of water, *J. Petrol.*, *49*, 841–855.

Behn, M. D., G. Hirth, and J. R. Elsenbeck II (2009), Implications of grain size evolution on the seismic structure of the oceanic upper mantle, *Earth Planet. Sci. Lett.*, *282*, 178–189.

Boatwright, J., J. B. Fletcher, and T. E. Fumal (1991), A general inversion scheme for source, site, and propagation characteristics using multiply recorded sets of moderate-size earthquakes, *Bull. Seismol. Soc. Am.*, *81*, 1754–1782.

Brune, J. N. (1970), Tectonic stress and spectra of seismic shear waves from earthquakes, *J. Geophys. Res.*, *75*, 4997–5009.

Cagnioncle, A. M., E. M. Parmentier, and L. T. Elkins-Tanton (2007), Effect of solid flow above a subducting slab on water distribution and melting at convergent plate boundaries, *J. Geophys. Res.*, *112*, B09402, doi:10.1029/2007JB004934.

Carcole, E., and H. Sato (2009), Spatial distribution of scattering loss and intrinsic absorption of short-period S waves in the lithosphere of Japan on the basis of the Multiple Lapse Time Window Analysis of Hi-net data, *Geophys. J. Int.*, *180*, 268–290.

Eberhart-Phillips, D. (1986), Three-dimensional velocity structure in northern California coast ranges from inversions of local earthquake arrival times, *Bull. Seismol. Soc. Am.*, *76*, 1025–1052.

Eberhart-Phillips, D., and M. Chadwick (2002), Three-dimensional attenuation model of the shallow Hikurangi subduction zone in the Raukumara Peninsula, New Zealand, *J. Geophys. Res.*, *107*(B2), 2033, doi:10.1029/2000JB000046.

Eshelby, J. D. (1957), The determination of the elastic field of an ellipsoidal inclusion and related problems, *Proc. R. Soc. London, Ser. A*, *241*, 376–396.

Faul, U. H., and I. Jackson (2005), The seismological signature of temperature and grain size variations in the upper mantle, *Earth Planet. Sci. Lett.*, *234*, 119–134.

Flanagan, M. P., and D. A. Wiens (1998), Attenuation of broadband P and S waves in Tonga: Observations of frequency dependent Q, *Pure Appl. Geophys.*, *153*, 345–375.

Gribb, T. T., and R. F. Cooper (2000), The effect of an equilibrated melt phase on the shear creep and attenuation behavior of polycrystalline olivine, *Geophys. Res. Lett.*, *27*, 2341–2344, doi:10.1029/2000GL011443.

Hacker, B. R., G. A. Abers, and S. M. Peacock (2003), Subduction factory 1. Theoretical mineralogy, densities, seismic wave speeds, and H_2O contents, *J. Geophys. Res.*, *108*(B1), 2029, doi:10.1029/2001JB001127.

Hasegawa, A., and J. Nakajima (2004), Geophysical constraints on slab subduction and arc magmatism, in *State of the Planet: Frontiers and Challenges in Geophysics*, Geophysical Monograph, vol. 150, edited by R. S. J. Sparks and C. J. Hawkesworth, pp. 81–94 , AGU, Washington, D. C.

Hasegawa, A., and A. Yamamoto (1994), Deep, low frequency microearthquakes in or around seismic low-velocity zones beneath active volcanoes in northeastern Japan, *Tectonophysics*, *223*, 233–252.

Hasegawa, A., N. Umino, and A. Takagi (1978), Double-planed structure of the deep seismic zone in the northeastern Japan arc, *Tectonophysics*, *47*, 43–58.

Hasegawa, A., D. Zhao, S. Hori, A. Yamamoto, and S. Horiuchi (1991), Deep structure of the northeastern Japan arc and its relationship to seismic and volcanic activity, *Nature*, *352*, 683–689.

Hasegawa, A., J. Nakajima, T. Yanada, N. Uchida, T. Okada, D. Zhao, T. Matsuzawa, and M. Umino (2013), Complex slab structure and arc magmatism beneath the Japanese Islands, *J. Asian Earth Sci.*, *78*, 277–290.

Honda, S., and T. Yoshida (2005), Application of the model of small-scale convection under the island arc to the NE Honshu subduction zone, *Geochem. Geophys. Geosyst.*, *6*, Q01002, doi:10.1029/2004GC000785.

Iwamori, H. (1998), Transportation of H_2O and melting in subduction zones, *Earth Planet. Sci. Lett.*, *160*, 65–80.

Iwata, T., and K. Irikura (1988), Source parameters of the 1983 Japan Sea earthquake sequence, *J. Phys. Earth*, *36*, 155–184.

Jackson, I., J. D. Fitz Gerald, U. H. Faul, and B. H. Tan (2002), Grain-size sensitive seismic wave attenuation in polycrystalline olivine, *J. Geophys. Res.*, *107*(B12), 2360, doi:10.1029/2001JB001225.

Jackson, I., U. H. Faul, J. D. Fitz Gerald, and B. H. Tan (2004), Shear wave attenuation and dispersion in melt-bearing olivine polycrystals: 1. Specimen fabrication and mechanical testing, *J. Geophys. Res.*, *109*, B06201, doi:10.1029/2003JB002406.

Karato, S. (2003), Mapping water content in the Earth's upper mantle, in *Subduction Factory*, edited by J. E. Eiler, pp. 135–152, AGU Monograph, Washington, D. C.

Katsumata, A. (2010), Depth of the Moho discontinuity beneath the Japanese islands estimated by traveltime analysis, *J. Geophys. Res.*, *115*, B04303, doi:10.1029/2008JB005864.

Kawakatsu, H., and S. Watada (2007), Seismic evidence for deep water transportation in the mantle, *Science*, *316*, 1468–1471.

Ko, Y. T., B. Y. Kuo, and S. H. Hung (2012), Robust determination of earthquakes source parameters and mantle attenuation, *J. Geophys. Res.*, *117*, B04304, doi:10.1029/2011JB008759.

Madariaga, R. (1976), Dynamics of an expanding circular fault, *Bull. Seismol. Soc. Am.*, *66*, 639–666.

Matsuzawa, T., A. Hasegawa, and A. Takagi (1989), Qp structure beneath the northeastern Japan arc estimated from spectral ratio method, *Tohoku Geophys. J.*, *32*, 21–33.

Mayeda, K., L. Malagnini, and W. R. Walter (2007), A new spectral ratio method using narrow band coda envelopes: Evidence for non-self-similarity in the Hector Mine sequence, *Geophys. Res. Lett.*, *34*, L11303, doi:10.1029/2007GL030041.

McCarthy, C., and Y. Takei (2011), Anelasticity and viscosity of partially molten rock analogue: Toward seismic detection of small quantities of melt, *Geophys. Res. Lett.*, *38*, L18306, doi:10.1029/2011GL048776.

Nakajima, J., and A. Hasegawa (2003), Estimation of thermal structure in the mantle wedge of northeastern Japan from seismic attenuation data, *Geophys. Res. Lett.*, *30*(14), 1760, doi:10.1029/2003GL017185.

Nakajima, J., T. Matsuzawa, A. Hasegawa, and D. Zhao (2001), Three-dimensional structure of V_p, V_s, and V_p/V_s beneath northeastern Japan: Implications for arc magmatism and fluids, *J. Geophys. Res.*, *106*, 21,843–21,857.

Nakajima, J., Y. Takei, and A. Hasegawa (2005), Quantitative analysis of the inclined low-velocity zone in the mantle wedge of northeastern Japan: A systematic change of melt-filled pore shapes with depth and its implications for melt migration, *Earth Planet. Sci. Lett.*, *234*, 59–70.

Nakajima, J., F. Hirose, and A. Hasegawa (2009), Seismotectonics beneath the Tokyo metropolitan area: Effect of slab-slab contact and overlap on seismicity, *J. Geophys. Res.*, *114*, B08309, doi:10.1029/2008JB006101.

Nakajima, J., K. Yoshida, and A. Hasegawa (2013a), An intraslab seismic sequence activated by the 2011 Tohoku-oki earthquake: Evidence for fluid-related embrittlement, *J. Geophys. Res. Solid Earth*, *118*, 3492–3505, doi:10.1002/jgrb.50426.

Nakajima, J., N. Uchida, T. Shiina, A. Hasegawa, B. R. Hacker, and S. H. Kirby (2013b), Intermediate-depth earthquakes facilitated by eclogitization-related stresses, *Geology*, *41*, 659–662.

Pozgay, S. H., D. A. Wiens, J. A. Conder, H. Shiobara, and H. Suguoka (2009), Seismic attenuation tomography of the Mariana subduction system: Implications for thermal structure, volatile distribution, and slow spreading dynamics, *Geochem. Geophys. Geosyst.*, *10*, Q04X05, doi:10.1029/2008GC002313.

Rietbrock, A. (2001), P wave attenuation structure in the fault area of the 1995 Kobe earthquake, *J. Geophys. Res.*, *106*, 4141–4154.

Roth, E. G., D. A. Wiens, L. M. Dorman, J. Hildebrand, and S. C. Webb (1999), Seismic attenuation tomography of the Tonga-Fiji region using phase pair methods, *J. Geophys. Res.*, *104*, 4795–4809.

Rychert, C. A., K. M. Fischer, G. A. Abers, T. Plank, E. Syracuse, J. M. Protti, V. Gonzalez, and W. Strauch (2008), Strong along-arc variations in attenuation in the mantle wedge beneath Costa Rica and Nicaragua, *Geochem. Geophys. Geosyst.*, *9*, Q10S10, doi:10.1029/2008GC002040.

Sano, Y., and J. Nakajima (2008), Geographical distribution of 3He/4He ratios and seismic tomography in Japan, *Geochem. J.*, *42*, 51–60.

Sato, H. (1992), Thermal structure of the mantle wedge beneath northeastern Japan: Magmatism in an island arc from the combined data of seismic anelasticity and velocity and heat flow, *J. Volcanol. Geotherm. Res.*, *51*, 237–252.

Sato, H., and M. Fehler (1998), *Seismic Wave Propagation and Scattering in the Heterogeneous Earth*, pp. 308 , Springer, New York.

Sato, T., and T. Hirasawa (1973), Body wave spectra from propagating shear cracks, *J. Phys. Earth*, *21*, 415–431.

Scherbaum, F. (1990), Combined inversion for the three-dimensional Q structure and source parameters using microearthquake spectra, *J. Geophys. Res.*, *95*, 12,423–12,438.

Shito, A., and T. Shibutani (2003), Anelastic structure of the upper mantle beneath the northern Philippine Sea, *Phys. Earth Planet. Inter.*, *140*, 319–329.

Shito, A., S. Karato, and J. Park (2004), Frequency dependence of Q in Earth's upper mantle inferred from continuous spectra of body waves, *Geophys. Res. Lett.*, *31*, L12603, doi:10.1029/2004GL019582.

Stachnik, J. C., G. A. Abers, and D. H. Christensen (2004), Seismic attenuation and mantle wedge temperatures in the Alaska subduction zone, *J. Geophys. Res.*, *109*, B10304, doi:10.1029/2004JB003018.

Takahashi, T. (2012), Three-dimensional attenuation structure of intrinsic absorption and wide-angle scattering of S waves in northeastern Japan, *Geophys. J. Int.*, *189*, 1667–1680.

Takahashi, T., H. Sato, M. Ohtake, and K. Obara (2005), Scale dependence of apparent stress for earthquakes along the subducting Pacific plate in northeastern Honshu, Japan, *Bull. Seismol. Soc. Am.*, *95*, 1334–1345.

Takanami, T., I. S. Sacks, and A. Hasegawa (2000), Attenuation structure beneath the volcanic front in northeastern Japan from broad-band seismograms, *Phys. Earth Planet. Inter.*, *121*, 339–357.

Takei, Y., and B. K. Holtzman (2009), Viscous constitutive relations of solid–liquid composites in terms of grain boundary contiguity: 1. Grain boundary diffusion control model, *J. Geophys. Res.*, *114*, B06205, doi:10.1029/2008JB005850.

Tamura, Y., Y. Tatsumi, D. Zhao, Y. Kido, and H. Shukuno (2002), Hot fingers in the mantle wedge: new insights into magma genesis in subduction zones, *Earth Planet. Sci. Lett.*, *197*, 105–116.

Tan, B. H., I. Jackson, and J. D. Fitz Gerald (1997), High-temperature viscoelasticity of fine-grained synthetic olivine aggregates, *Geophys. Res. Lett.*, *24*, 1055–1058.

Tanaka, A., M. Yamano, Y. Yano, and M. Sasada (2004), Geothermal gradient and heat flow data in and around Japan (I): Appraisal of heat flow from geothermal gradient data, *Earth Planets Space*, *56*, 1191–1194.

Torii, Y., and S. Yoshioka (2007), Physical conditions producing slab stagnation: Constraints of the Clapeyron slope, mantle viscosity, trench retreat, and dip angles, *Tectonophysics*, *445*, 200–209.

Tsuji, Y., J. Nakajima, and A. Hasegawa (2008), Tomographic evidence for hydrated oceanic crust of the Pacific slab beneath northeastern Japan: Implications for water transportation in subduction zones, *Geophys. Res. Lett.*, *35*, L14308, doi:10.1029/2008GL034461.

Tsumura, N., A. Hasegawa, and S. Horiuchi (1996), Simultaneous estimation of attenuation structure, source parameters and site response spectra – application to the northeastern part of Honshu Japan, *Phys. Earth Planet. Inter.*, *93*, 105–121.

Tsumura, N., S. Matsumoto, S. Horiuchi, and A. Hasegawa (2000), Three-dimensional attenuation structure beneath the northeastern Japan arc estimated from spectra of small earthquakes, *Tectonophysics*, *319*, 241–260.

Uchida, N., T. Matsuzawa, W. L. Ellsworth, K. Imanishi, T. Okada, and A. Hasegawa (2007), Source parameters of a M4.8 and its accompanying repeating earthquakes off Kamaishi, NE Japan: Implications for the hierarchical structure of asperities and earthquake cycle, *Geophys. Res. Lett.*, *34*, L20313, doi:10.1029/2007GL031263.

Umino, N., and A. Hasegawa (1984), Three-dimensional Qs structure in the northeastern Japan arc (in Japanese with English abstract), *J. Seismol. Soc. Jpn*, *37*, 217–228.

Wada, I., M. D. Behn, and J. He (2011), Grain-size distribution in the mantle wedge of subduction zones, *J. Geophys. Res.*, *116*, B10203, doi:10.1029/2011JB008294.

Wessel, P., and W. H. F. Smith (1998), New, improved version of the Generic Mapping Tools released, *Eos Trans. AGU*, *79*, 579.

Wiens, D. A., J. A. Conder, and U. H. Faul (2008), The seismic structure and dynamics of the mantle wedge, *Annu. Rev. Earth Planet. Sci.*, *36*, 421–455.

Yoshioka, S., M. Toda, and J. Nakajima (2008), Regionality of deep low-frequency earthquakes associated with subduction of the Philippine Sea plate along the Nankai Trough, southwest Japan, *Earth Planet. Sci. Lett.*, *272*, 189–198.

Zhao, D., A. Hasegawa, and S. Horiuchi (1992), Tomographic imaging of P and S wave velocity structure beneath northeastern Japan, *J. Geophys. Res.*, *97*, 19,909–19,928.

Zhao, D., T. Yanada, A. Hasegawa, N. Norihito, and W. Wei (2012), Imaging the subducting slabs and mantle upwelling under the Japan Islands, *Geophys. J. Int.*, *190*, 816–828.